

Zeolite membrane with sub-nanofluidic channels for superior blue energy harvesting

Received: 7 November 2023

Accepted: 21 November 2024

Published online: 02 December 2024

Ruicong Wei ^{1,2}, Xiaowei Liu ^{1,2}, Li Cao ¹, Cailing Chen ¹, I-Chun Chen¹, Zhen Li¹, Jun Miao ¹ & Zhiping Lai ¹ ✉

Blue energy, a clean energy source derived from salinity gradients, has recently drawn increased research attention. It can be harvested using charged membranes, typically composed of amorphous materials that suffer from low power density due to their disordered structure and low charge density. Crystalline materials, with inherently ordered porous structures, offer a promising alternative for overcoming these limitations. Zeolite, a crystalline material with ordered sub-nanofluidic channels and tunable charge density, is particularly well-suited for this purpose. Here, we demonstrate that NaX zeolite functions as a high-performance membrane for blue energy generation. The NaX zeolite membrane achieves a power density of 21.27 W m^{-2} under a 50-fold NaCl concentration gradient, exceeding the performance of state-of-the-art membranes under similar conditions. When tested under practical scenarios, it yields power densities of 29.1 W m^{-2} , 81.0 W m^{-2} , and 380.1 W m^{-2} in the Red Sea/River, Dead Sea/River, and Qinghai Brine/River configurations, respectively. Notably, the membrane operates effectively in high alkaline conditions ($\sim 0.5 \text{ M NaOH}$) and selectively separates CO_3^{2-} from OH^- ions with a selectivity of 25. These results underscore zeolite membranes' potential for blue energy, opening further opportunities in this field.

The energy crisis and its associated climate change have been global concerns for the past two decades. To address these issues, significant research efforts have been focused on exploring and utilizing renewable energy resources. One such area of research is blue energy, also known as osmotic power, which utilizes cation/anion selective membranes to generate electricity from a salt gradient. Various amorphous materials, including polymers¹, silk nanofibril², silica³, and hydrogel⁴, have been extensively studied and have shown promising performances. However, these materials suffer from low power density generation due to the presence of disordered channels, resulting in higher cation/anion transport resistance. In the past five years, studies have emerged regarding the potential of two-dimensional (2D) materials, such as COFs^{5,6}, MXene⁷, and graphene oxide⁸, in osmotic power generation. Notably, COFs with their ordered 2D nanofluidic channels have demonstrated promising results in terms of energy density generation, suggesting that

ordered structures with nanoscale channels can significantly enhance energy conversion efficiency.

While materials with nanochannels (channel size: 1–100 nm) have been extensively investigated, the exploration of crystalline materials with sub-nanochannels (channel size $< 1 \text{ nm}$) for blue energy conversion is relatively limited. In principle, sub-nanochannels with high charge density can be favorable for achieving high-performing osmotic power generation. These sub-nanochannels, slightly larger than hydrated ions such as Na^+ , K^+ , and Cl^- , can ensure high cation/anion selectivity by maximizing surface diffusion. Similar channels have been observed in biological systems, such as the “sodium-potassium pump” in all animal cells⁹ and electrical generation cells in eels¹⁰, which exhibit selective cation/anion transport. Inspired by these natural phenomena, research has been conducted to study metal-organic framework (MOF)-based membranes for ion separation¹¹ and osmotic power generation^{12–14}.

¹Advanced Membranes and Porous Materials Center, Division of Physical Science and Engineering, King Abdullah University of Science and Technology (KAUST), Thuwal 23955-6900, Saudi Arabia. ²These authors contributed equally: Ruicong Wei, Xiaowei Liu. ✉ e-mail: zhiping.lai@kaust.edu.sa

Zeolites, a type of silicate/aluminosilicate material with crystalline microporous structures, have found widespread industrial applications in areas such as adsorption and catalysis^{15,16}. Zeolite membranes for molecular separations¹⁷ and solvent dehydration¹⁸ have also been extensively investigated. In particular, NaA zeolite has been commercialized for solvent dehydration, demonstrating the scalability of zeolites for real industrial applications¹⁹. This membrane is the first and only commercialized membrane with ordered crystalline microporous structures. In recent years, the application of zeolite has been extended to applications regarding energy storage. For example, a recent report published in Nature demonstrated that NaX zeolite can be utilized as a solid electrolyte in high-performing lithium-air batteries²⁰. Compared to other porous crystalline materials such as MOFs or COFs, zeolites possess several advantages, including high hydrothermal and chemical stability, cost-effective synthesis, and proven industrial-scale production¹⁹.

In terms of osmotic power generation, zeolites with high framework Al content could induce a high charge density, which is an important attribute for this application. It is known that zeolite consists of tetrahedrally coordinated silicon (SiO₄) and aluminum (AlO₄) alternatively connected by bridging oxygen. Depending on the zeolite type, this primary structural building unit will further connect in a specific way to form a unique 2D or 3D framework structure with microporous channels. In principle, a zeolite with all silicate would have a neutral framework without any charge. In contrast, for aluminosilicate zeolite, each Al introduced in the framework will induce a negative charge near its coordination center (Fig. 1a). The negative charge is balanced by an extra-framework cation near the AlO₄ to make the material charge neutral. It means the higher the Al content (i.e., lower Si/Al ratio), the higher the zeolite ion exchange capacity (IEC), which is an important attribute for high-performing osmotic power generation. Taking NaX as an example, this material has a Si/Al ratio of 1–1.5^{21,22}, the lowest beside NaA in zeolites. The IEC based on this Si/Al ratio range is between 7.13 and 5.71 mmol g⁻¹, outperforming all the reported materials so far. Such high IEC also infers a high surface charge density, which is determined to be –200 mC m^{-2,23}. Structurally, NaX has a FAU framework composed of two types of cages: sodalite (SOD or β cage) and supercages. The inside cage diameter of the former is 0.63 nm, and the latter is 1.12 nm. The SOD cages are interconnected by hexagonal 6-membered ring window of 0.23 nm to form supercages with 12-membered ring windows of 0.74 nm along [111] direction²¹ (Fig. 1b). These supercages connect along [110] direction and form large straight sub-nanofluidic channels for molecule transport (Fig. 1c). The Al-induced negative surface charges are distributed inside the channels at different sites. Potentially, these negative charges could selectively attract cation ions to pass through while reject anions, rendering cation/anion separation. Combining its high charge density and outstanding porosity (BET surface area: ~700 m² g⁻¹)²⁴, we hypothesize that NaX zeolite membrane can be a promising candidate for blue energy conversion through reverse electrodialysis. However, its application in this context has not been explored so far.

Despite the proven industrial viability of zeolite membranes, they are known to suffer from mechanical fragility due to their intrinsic crystalline structure. This phenomenon is also observed in other crystalline materials like MOFs or COFs. To address this issue, our research group has developed a strategy that utilizes carbon nanotubes (CNTs) as a support layer to enhance the mechanical stability of membranes composed of fragile materials, such as conjugated microporous polymers²⁵ and ZIF-8²⁶. This strategy can be potentially applied to zeolite membranes to improve their mechanical properties.

In a concept-proof study, we fabricated a flexible NaX zeolite membrane using CNTs as the support material. The resulting membrane exhibits a sandwich structure with CNTs as the middle layer, imparting superior flexibility while retaining its mechanical integrity. A series of fundamental studies demonstrated that the membrane

possesses high cation/anion selectivity (e.g., K⁺/Cl⁻, Na⁺/Cl⁻) and surface charge density. These properties contribute to an osmotic power generation of 21.27 W m⁻² for a 50-fold NaCl concentration gradient, surpassing the performance of most reported membranes so far under the same concentration gradient. The membrane was also tested under various conditions, including Red Sea/river, Dead Sea/river, and Qinghai Brine/river, yielding power densities of 29.1 W m⁻², 81.0 W m⁻², and 380.1 W m⁻², respectively. Such osmotic generation outperforms most of the start-of-art membranes reported. Particularly noteworthy is the membrane's capability to operate in highly basic solutions, exhibiting a CO₃²⁻/OH⁻ selectivity of approximately 25.31, showcasing its potential for applications involving highly alkaline solutions.

Results

Membrane synthesis and characterization

We prepared the membrane on a CNT-supported polysulfone (PES) substrate (pore size: 0.2 μ m) using a conventional hydrothermal method (see methods, Supplementary Fig. 1). The zeolite membrane successfully formed on the CNT support and was named ZC membrane hereafter. To confirm its structure, an X-ray diffraction analysis (XRD) measurement was conducted, as shown in Fig. 2a. The XRD pattern shows all the characteristic peaks compared with the simulated NaX zeolite pattern, confirming the successful formation of the zeolite framework structure. The absence of foreign peaks and the high peak sharpness suggest that a pure and highly crystalline NaX zeolite membrane was formed. The morphology of the membrane was studied by scanning electron microscope (SEM) imaging (Fig. 2b, c, Supplementary Figs. 2, 3) and atomic force microscope (AFM) analysis (Supplementary Fig. 4). It is clear that a continuous and dense membrane was formed. The front view of the SEM image (Fig. 2b) indicates that the membrane was mainly composed of closely intergrown octahedral crystals of ~700 nm. The cross view (Fig. 2c, Supplementary Fig. 3d–j) shows the membrane has a sandwich structure with the zeolite layer at the sides to pack the CNT layer in the middle. A closer look at the middle layer found it was composed of a CNT-zeolite composite. This sandwich structure could be the main attribute that enables the zeolite membrane to be mechanically strong under bending force (Fig. 2d). It is known that CNT intrinsically has exceptionally high mechanical strength, stiffness, and flexibility, making it an attractive material for composite materials to reduce the brittleness of nanocrystalline ceramics (e.g., Al₂O₃, SiO₂). It has been found a properly formed CNT-ceramic composite could improve the fracture toughness and bending strength by 300%²⁷ and 65%²⁸, respectively. These studies explained well the ZC membrane obtained in this study could sustain its mechanical integrity in flexible status under bending force (Supplementary Movies 1). To further understand the membrane's structure at the microscopic scale, the membrane was examined by high-resolution transmission electron microscopy (HRTEM) imaging analysis (Fig. 2e), showing an FAU porous structure along [110] orientation at high resolution with a distinct fast-Fourier-transform (FFT) pattern. The sub-nanofluidic channel was clearly observed along this direction. This channel mainly functioned for ion transport in osmotic power generation.

The ion transport within the sub-nanofluidic channel was also highly influenced by the chemical compositions of the membrane, which were carefully studied by X-ray photoelectron spectroscopy (XPS) (Supplementary Fig. 5), Raman spectroscopy (Supplementary Fig. 6), Fourier transform infrared (FTIR) (Supplementary Fig. 7) and Nuclear Magnetic Resonance (NMR) spectroscopy (Fig. 2f) analysis. XPS spectra show the presence of Si-O, Al-O, and Na-O groups in the membrane²⁹. The detailed local chemical groups and structures were further investigated by Raman and FTIR. Both spectra show the characteristic peaks of NaX, proving zeolite formation. Raman bands at 374 cm⁻¹ and 504 cm⁻¹ were assigned to the bending mode of framework 6-membered ring and 4-membered ring, respectively³⁰, while

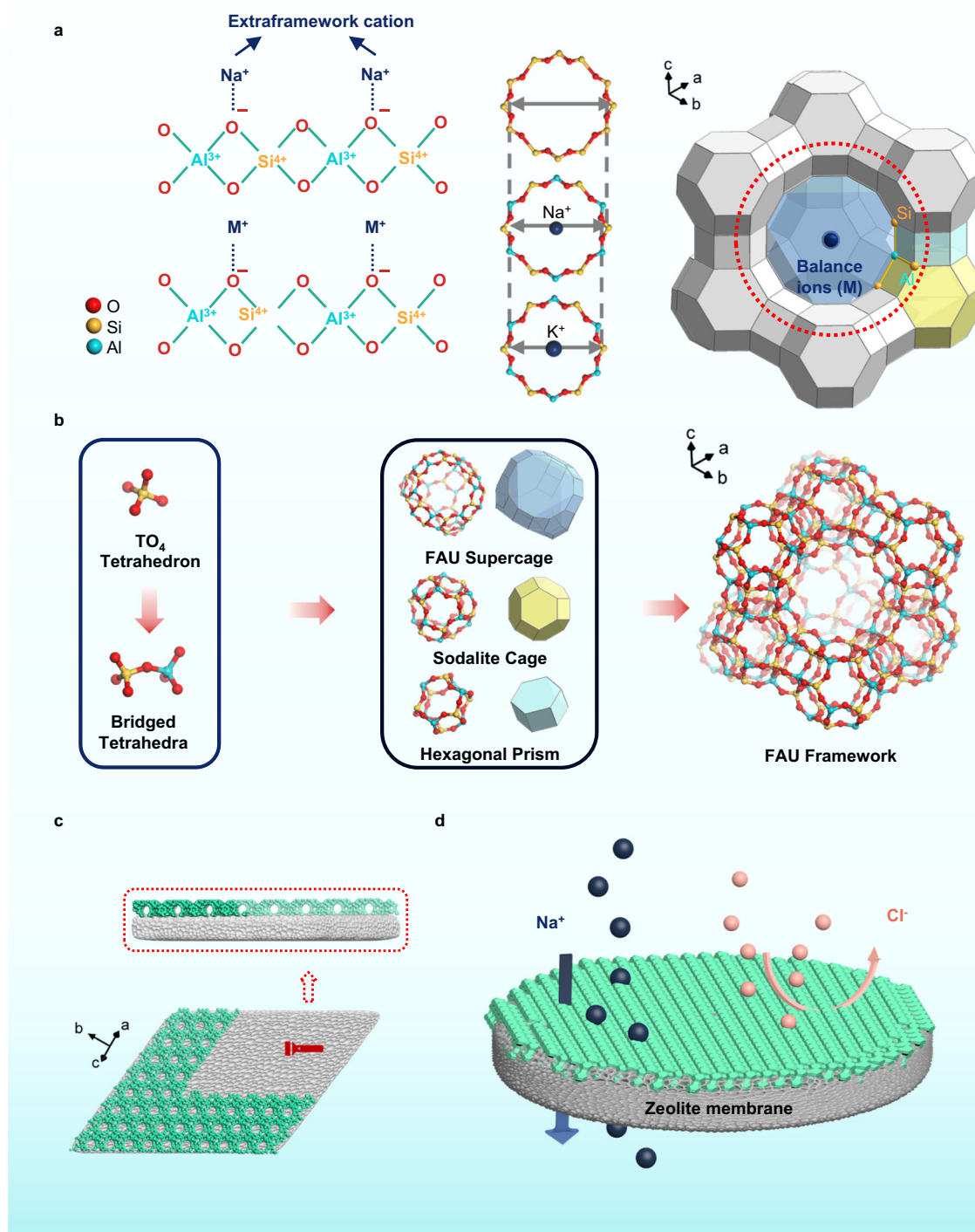


Fig. 1 | Schematic illustration of surface charge and structure of NaX zeolite membrane. **a** A demonstration of tetrahedrally coordinated silicon (SiO₄) and aluminum (AlO₄) alternatively connected by bridging oxygen. The negative charges caused by aluminum introduction are balanced by extra-framework sodium (Na⁺). These negative charges could also be compensated by other types of monovalent cations (M⁺) or divalent cations (M²⁺). **b** Tetrahedra SiO₄ and AlO₄ form sodalite cages which are then connected to form FAU supercages. There are three location

sites (I, II, III) for charge balancing cations in the super cage⁴⁹. **c** The top image demonstrates the cross-section of a zeolite membrane supported on a porous substrate with a certain thickness. The bottom image shows NaX zeolite sub-nanofluidic channels along [110] orientation. **d** The image shows the NaX zeolite selectively allows cations (e.g., Na⁺) to pass through the membrane and reject anions (Cl⁻), showing a visualized process for a cation/anion selective membrane process.

broad bands at 1000 cm⁻¹ and 1095 cm⁻¹ are attributed to the stretching vibration of SiO₄/AlO₄ tetrahedra. For the FTIR spectra, the 557 cm⁻¹ and 662 cm⁻¹ peaks uniquely appeared in the zeolite material and were assigned to double ring vibration and Si-O/Al-O symmetrical stretch, respectively^{31,32}. The FTIR peak shift of 662 cm⁻¹ was used to

obtain the overall Si/Al ratio^{33–35} and was found to be -1.2, which is in the range of a typical NaX zeolite. To determine the framework Si/Al ratio, NMR analysis (Fig. 2f) was conducted. For a typical zeolite NMR spectral, the signal at 50–70 ppm corresponds to tetrahedrally coordinated Al in the zeolite framework (AlO₄)³⁶. The non-framework Al in

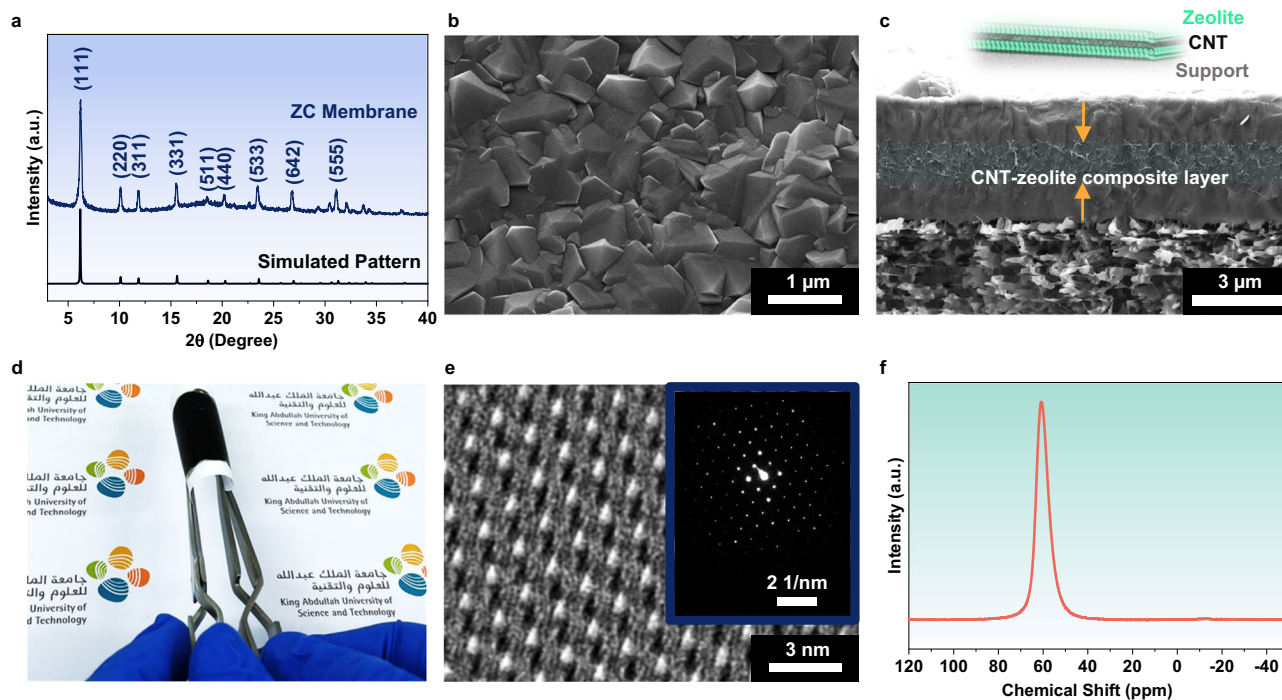


Fig. 2 | Characterization of the NaX zeolite membrane grown on CNT support. **a** The XRD pattern of the ZC membrane is compared with a simulated pattern of NaX zeolite, whose CIF file was obtained from the International Zeolite Association. The characteristic peaks of NaX are labeled. SEM images of **(b)** front view and **(c)** cross view show the morphology and thickness of the ZC membrane. A cross-view SEM image indicates the ZC membrane is a sandwich structure with the middle layer formed as a CNT-zeolite composite. The photograph image in **(d)** shows the

ZC membrane under bending force. **e** HRTEM image of the ZC membrane shows the sub-nanofluidic channel of the membrane along [110] direction. The inserted SAED pattern highlights the high crystallinity of the membrane. **f** NMR pattern of ZC membrane. Only one band at -60.5 ppm was observed and assigned to tetrahedrally coordinated AlO_4 in the zeolite framework. This result confirms all the Al in the ZC membrane has been incorporated into the zeolite framework.

the form of octahedral coordination (AlO_5) will cause a signal at 0 ppm³⁶. In some zeolite samples, signals at 30 – 50 ppm could be observed and were possibly caused by non-framework Al species in the state of tetrahedral- or penta-coordination³². In the NMR spectra (Fig. 2f) of our sample, only one signal sitting at -60.5 ppm was observed, and no peaks were observed between 0 and 50 ppm, proving all Al species in the membrane have been incorporated into the zeolite framework. Coupled with the overall Si/Al ratio determined from Supplementary Fig. 7, we confirmed that the membrane has a framework Si/Al ratio of -1.2 , with a corresponding IEC of -6.49 mmol g^{-1} . To the best of our knowledge, this capacity is the highest among all the membranes reported for osmotic power generation so far. Such high IEC also guarantees a high surface charge density of the membrane for selective ion transport. To achieve a better understanding of this membrane's potential for osmotic power generation, we did a Molecular dynamics (MD) simulation on the pure zeolite membrane to see the cations/anions transport across the NaX zeolite (Fig. 3).

MD simulation of ion transport

The MD simulation was conducted by fitting the pure zeolite membrane in a simulation box which was filled with NaCl or KCl electrolyte with a concentration gradient across the membrane (Fig. 3a). After some simulation time, the number of ions transported through the membrane was counted. Based on this simulation, we first calculated the potential of the mean force (PMF) profile for cations (Fig. 3b, Supplementary Fig. 8a) and anions (Fig. 3c, Supplementary Fig. 8b) from the ion density distribution profile (Supplementary Fig. 9). At any concentration gradient in NaCl electrolyte, the energy barrier for Na^+ to pass through the membrane was ranged from -0.16 to -9.9 kJ mol^{-1} (Fig. 3b) while the energy barrier for Cl^- was unlimited large due to the

strong repulsive force (Fig. 3c) between the negatively charged zeolite surface and Cl^- . Similar behavior was also observed for the membrane in KCl electrolyte at the concentration gradient of 0.5 M/ 0.01 M. Such a high difference in energy barrier between cations and anions results in the Na^+ (Fig. 3d, Supplementary Fig. 10) or K^+ (Fig. 3e) passing through the membrane to the lower concentration side while Cl^- was fully rejected. At higher concentration gradient (2 M/ 0.01 M or 5 M/ 0.01 M) in KCl electrolyte, the energy barrier for Cl^- was still one order of magnitude higher than K^+ , creating a large K^+/Cl^- selectivity (Supplementary Fig. 11). The simulation results tell that the membrane exhibited a superior cation/anion selectivity due to high negative charge density, which implies NaX membrane has a high potential for osmotic power generation. In the following, we experimentally studied the ion transport properties in the synthesized ZC membrane to further verify its capability in this application.

Characterizations of ion transport properties

The transmembrane ionic transport properties of the ZC membrane were studied by current (I)-voltage (V) measurements using a pair of Ag/AgCl electrodes with salt bridges and a homemade electrochemical device (Supplementary Fig. 12). We selected potassium chloride (KCl) as the standard electrolyte as K^+ and Cl^- have similar diffusion coefficients³⁷. Such electrolytes can minimize the effects of the ions' intrinsic diffusion rate difference on the cation/anion selectivity across the membrane. I-V measurement was first conducted by subjecting the membrane to a KCl electrolyte with zero concentration gradient. The electrolyte concentrations varied from 1 M to 10^{-6} M. The I-V response for all concentrations shows a linear ohmic behavior (Supplementary Fig. 13a), indicating the membrane has a symmetric microstructure^{7,38} which corresponds well with the morphology observed from SEM analysis (Fig. 2c). Calculating the slope of these linear I-V curves gives

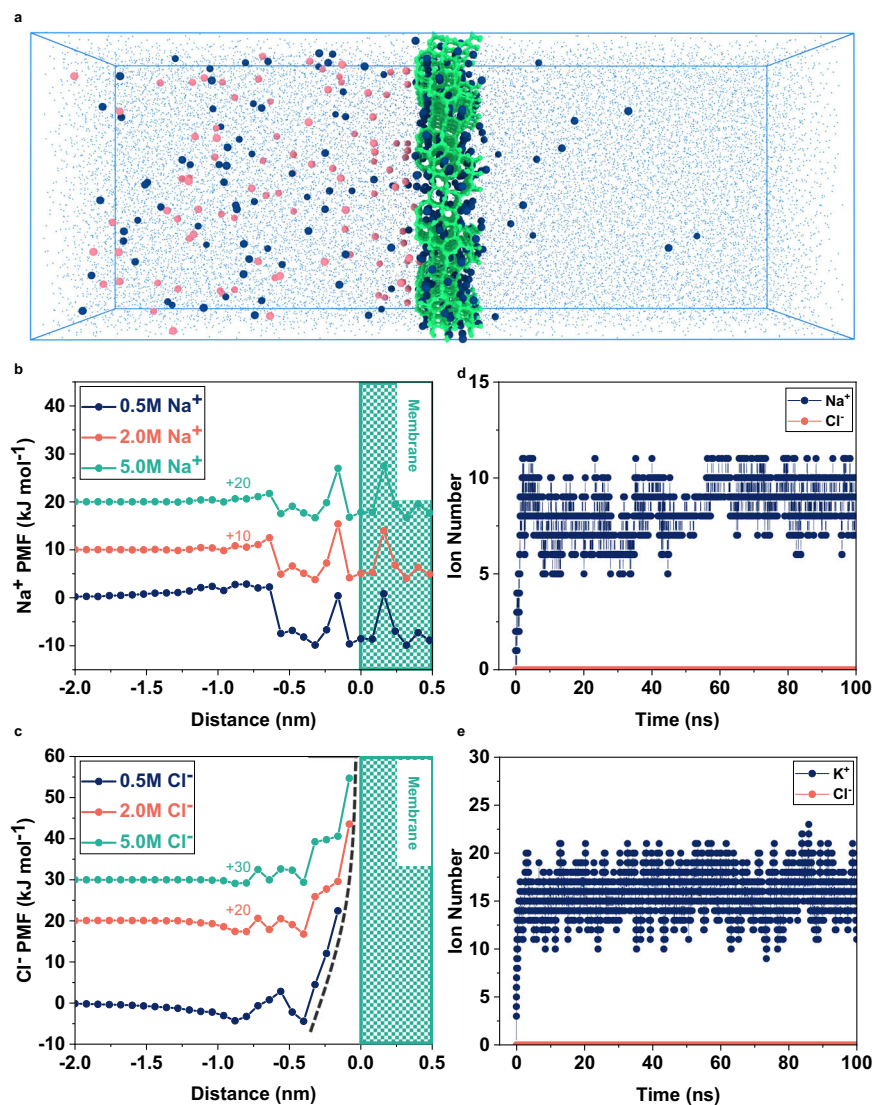


Fig. 3 | MD simulation of cations/anions transport across NaX zeolite membrane. **a** An illustrative diagram showing the simulation box with NaX zeolite membrane in the middle. The left side of the membrane was filled with concentrated NaCl or KCl electrolyte, while the right side was filled with the same electrolyte as the left but at a lower concentration (0.01M) to create a concentration gradient across the membrane. The blue filled circles represent Na⁺ while the pink filled circles represent Cl⁻. **b** and **(c)** are PMF profiles of Na⁺ and Cl⁻,

respectively, at different electrolyte concentrations. The green shaded area in **b** and **(c)** represent the ZC membrane. The black dashed line in **(c)** represents the unlimited energy barrier for Cl⁻ to pass through the membrane. **d** and **(e)** are graphs demonstrating the number of ions transported across the membrane versus simulation time from the concentrated side to the diluted side at a concentration gradient of 0.5M/0.01M. **d** shows the performance in NaCl electrolyte while **(e)** in KCl electrolyte.

the conductance of this symmetric membrane at different electrolyte concentrations (Fig. 4a). The conductance started to deviate from the bulk value when the concentration was below 0.1M, suggesting ion transport across the ZC membrane was governed by surface charge. The surface charge density ($\sigma_{D,zp}$) can be estimated by zeta potential and was calculated to be -9.65 mC m^{-2} (see methods). A particular note here is $\sigma_{D,zp}$ only gives the effective surface charge on the particles of the membrane and ignores the charges inside the porous sub-nanofluid channels throughout the whole membrane. To obtain the overall surface charge density σ_D , a potentiometric titration method was used and determined to be -201 mC m^{-2} ^{23,39}, which is higher than any reported values so far⁴⁰. Such extraordinary surface charge density is closely related to the high IEC (6.49 mmol g⁻¹), which directly results from the low framework Si/Al ratio (-1.2). The low Si/Al ratio enables a highly negatively charged surface in the sub-nanofluidic channels, which selectively attract and allow cations to diffuse through while

rejecting anions. If a concentration gradient was applied, the cations would diffuse from the high-concentration to the low-concentration side, leading to a directional ions flow. To retain the electrolyte solutions' electroneutrality, redox reactions would happen on the Ag/AgCl electrode surfaces and transfer electrons through an external circuit. In such a setup, the Gibbs free energy of the concentration gradient can be harvested and converted to electricity via the membrane process. To investigate this cation-selective transport behavior, we measured the I-V response under a series of concentration gradients using KCl as the electrolyte. The osmotic potential (V_{os}) and current (I_{os}) can be directly obtained from the intercept of the zero-axis on the I-V curve as the redox potential (V_{redox}) of electrodes has been eliminated by the saturated KCl salt bridge (Supplementary Fig. 12d, e). The ZC membrane has a V_{os} of 94 mV and an I_{os} of 118 μA under a 50-fold gradient (Fig. 4b). This osmotic potential gives a K⁺/Cl⁻ selectivity of -40 corresponding a cation transference numbers (t^+) of 0.96 which is much

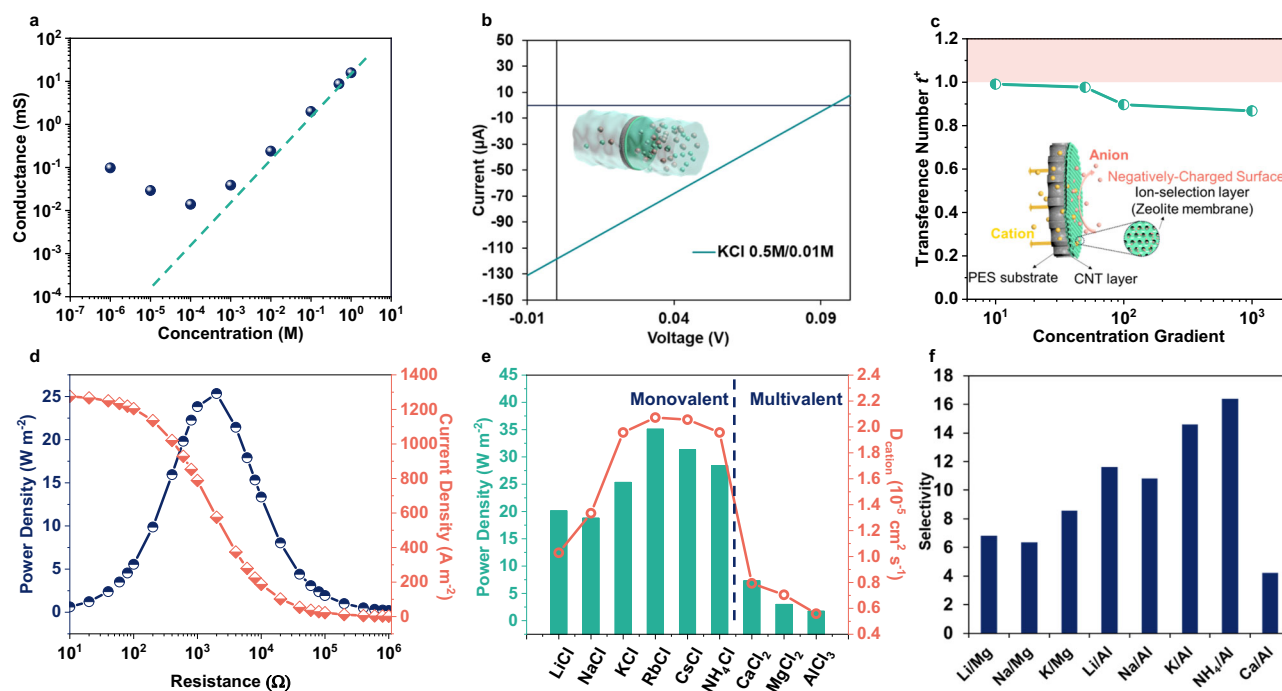


Fig. 4 | Fundamental analysis of cation/anion separation performance for osmotic power generation. **a** A graph of conductance versus KCl electrolyte concentration of ZC membrane. The dashed line in the graph shows the conductance behavior in the bulk solution of high concentrations. **b** The I-V curve showing osmotic I_{os} and V_{os} of ZC membrane in a 50-fold concentration gradient of KCl electrolyte. The horizontal and vertical lines in the graph represent the zero points of current and potential, respectively. The inserted image illustrates the configuration of the membrane testing. **c** Transference number t^+ calculated based on measured V_{os} versus different concentration gradients of KCl electrolyte. The inserted image illustrates the mechanism of the cation/anion separation within the membrane. The pink-shaded area is intended solely to highlight the green line

graph in the middle section and holds no scientific significance. **d** Osmotic power density and current density of the ZC membrane (effective area: $\sim 0.03 \text{ mm}^2$) tested by connecting the electrochemical cell to an external loader in a 50-fold concentration gradient of KCl electrolyte. **e** The green columns showing osmotic power density obtained in electrolytes of various cations under a 50-fold concentration gradient. The pink graph is the corresponding cation diffusion coefficient. **f** Selectivities of different cations obtained based on the osmotic power density according to the previous work^{5,14}. The cation-anion selectivity of different cations relative to Cl^- lead to varied osmotic power density which can be used to calculate the different cation-cation selectivity.

greater than 0.5 and approaches to 1. It implies the ion conducting across the ZC membrane is mainly accomplished by the K^+ cations, demonstrating the highly cation-selective property of the ZC membrane. Such selectivity is mainly attributed to the negatively charged sub-nanofluidic channels within the FAU framework of the membrane. To further confirm this, we conducted a controlled experiment by fabricating a 'defective' membrane so that ions could pass through via the membrane defects (e.g., inter-particle space, micro-cracks) and tested its ion transport properties (Supplementary Fig. 14). The membrane shows no osmotic voltage under of 50-fold KCl gradient, confirming it is the sub-nanofluidic channels within FAU framework that function for the osmotic power generation, hence the high cation transference number t^+ . The t^+ value slightly declined from 0.99 to 0.87 as the concentration gradient rose from 10 to 1000 (Fig. 4c). Similarly, the maximum power conversion efficiency (η) calculated from t^+ decreased from 48% to 27% (Supplementary Fig. 15). These phenomena have also been observed for other reported membranes^{2,41,42} and might be attributed to the varied surface charge on the membrane induced by the concentration gradient⁴³.

Effects of cations on osmotic power generation

The osmotic power generation property of the ZC membrane was tested by connecting the homemade electrochemical device to an external circuit with a resistor load (RL). The testing was conducted under a 50-fold concentration gradient in KCl electrolyte (Fig. 4d). The membrane exhibited a typical osmotic behavior in which current density gradually decreased as resistance increased while the power density displayed a pattern similar to Gaussian distribution with a

maximum power of 25.3 W m^{-2} occurred near the medium current density. The obtained power is the highest among the sub-nanofluidic materials^{14,44} and outperformed most reported membranes (Supplementary Table 4) under the same testing conditions (i.e., membrane area, KCl electrolyte, 50-fold concentration gradient). Such impressive performance was mainly contributed by the combined effects of high surface charge density, excellent porosity (BET surface area: $711.4 \text{ m}^2 \text{ g}^{-1}$), and crystalline sub-nanofluidic channels within the zeolite structure of the ZC membrane since the CNT-PES substrate only has a negligible power density of 0.83 W m^{-2} (Supplementary Fig. 16). To further understand the membrane's performance, we tested the osmotic power generation at different cation electrolytes (Supplementary Fig. 17). Overall, the osmotic power of monovalent cations was at least 3 times higher than multivalent cations (Fig. 4e, green columns). This observation could be due to the fact that the cation diffusion coefficients D_{cation} of monovalent cations are much higher than multivalent cations (Fig. 4e, pink graph). The trend of diffusion coefficients is also closely correlated with the osmotic power of monovalent cations with the peak value sitting at RbCl (power density, 35.1 W m^{-2}). This trend suggests that the cations tested can freely transport within the sub-nanofluidic channels of the ZC membrane relative to Cl^- , leading to relatively poor cation-cation sieving effects (Fig. 4f). This observation is mainly due to that the membrane has a window size of $\sim 0.74 \text{ nm}$ (Supplementary Fig. 18) which is higher than the hydrated cations tested (Supplementary Table 2) except Al^{3+} (hydrated size, $\sim 0.75 \text{ nm}$). Thus, the ZC membrane can sieve all the cations from Al^{3+} with a selectivity higher than 10 (Fig. 4f). Such selective performance inspired us, though contrary to common

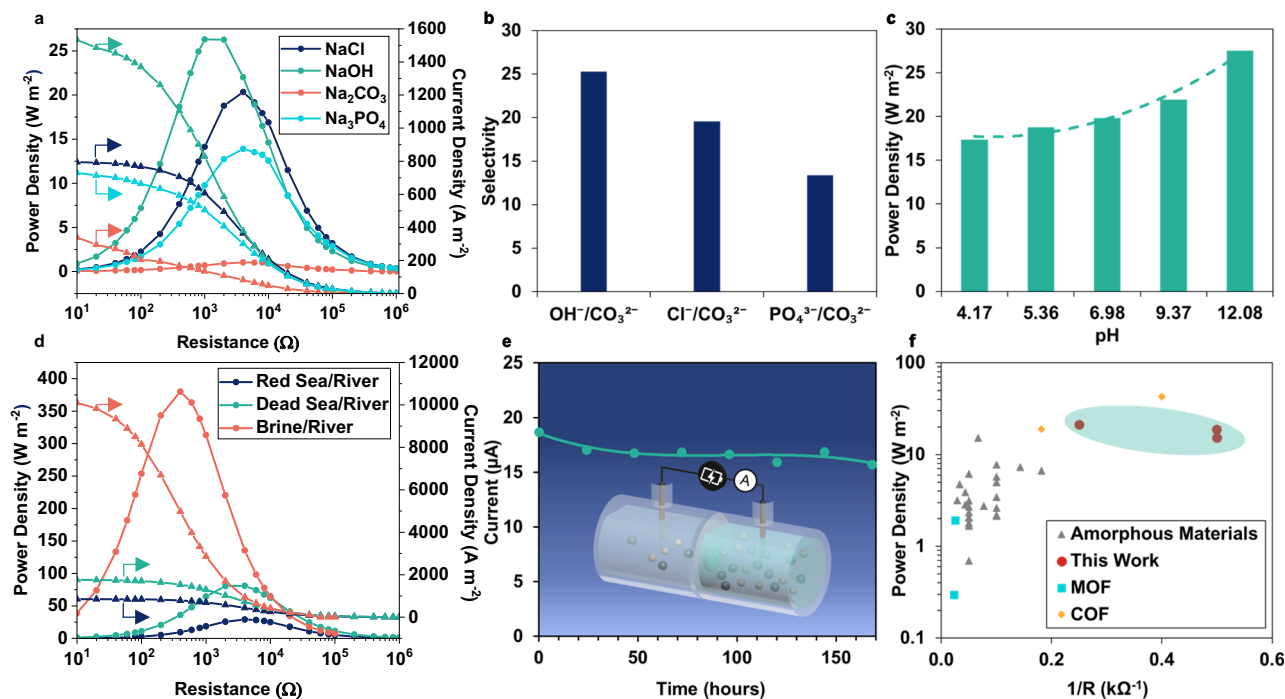


Fig. 5 | Effects of different conditions on osmotic power generation. **a** Osmotic power density and current density of ZC membrane tested in NaCl, NaOH, Na₂CO₃, and Na₃PO₄ electrolytes under a 50-fold concentration gradient. **b** Selectivities of CO₃²⁻ against OH⁻, Cl⁻, and PO₄³⁻ based on osmotic output^{6,14}. The cation-anion selectivity of Na⁺ relative to various anions leads to varied osmotic power density which can be used to calculate the different anion-anion selectivity. **c** Effects of pH on osmotic power density obtained in NaCl electrolyte of a 50-fold concentration gradient. The green dashed line represents the guided increasing trend of power density as a function of pH. **d** Osmotic power density and current density of ZC

membrane tested in Red Sea/River, Dead Sea/River, and Qinghai Brine /River waters. **e** Current output in artificial seawater/river water of ZC membrane measured at an external resistance of 0.4 kΩ in seven days of operation. The inserted image illustrates the experiment-setup for the stability test. **f** The plot of reported power density versus the reciprocal of external resistance load at the maximum power achieved. The data points were selected as they were measured under the same conditions (0.5 M:0.01 M NaCl electrolyte) across the same membrane area. The associated references of these data points were listed in Supplementary Table 4.

intuition, to study if the membrane can separate anions and perform differently via manipulating electrolyte anions.

Effects of anions on osmotic power generation

In principle, the ZC membrane, on the one hand, has a negatively charged surface that will naturally repel anions in the ion transport to achieve cation/anion separation. On the other hand, these anions have diverse polarity and hydration status, inducing different interaction strengths with the charged surface. This interaction could directly affect the diffusion rate across the membrane, achieving different cation/anion selectivity and osmotic power. To prove this hypothesis, we first studied the transmembrane ion transport properties of the ZC membrane in NaCl electrolyte as a benchmark. The I-V curves (Supplementary Fig. 19), though not identical, are quite similar to observations in the KCl electrolyte. The slightly lower transference number (t^+) of 0.92 was mainly due to the smaller diffusion coefficient of Na⁺ as compared with K⁺. Nevertheless, the ZC membrane achieved a power density of 20.3 W m⁻² in a 50-fold (0.5 M:0.01 M) NaCl electrolyte, which is under the standard artificial seawater/river water condition. We then tested the membrane in Na⁺ electrolytes with different counter anions (NaBr, NaI, NaF, NaOH, NaNO₃, Na₂S, Na₂SO₄, Na₂CO₃, Na₃PO₄) under the same concentration gradient (Supplementary Fig. 20, Fig. 5a, Supplementary Fig. 21). Similar to cation series (Fig. 4e), power densities obtained from monovalent anions are, in general, at least twice higher than those of multivalent anions (Supplementary Fig. 21). This observation could be due to the hydration energies ($\Delta_{\text{hyd}}G^\circ$) of these anions (Supplementary Table 3)⁴⁵. The $\Delta_{\text{hyd}}G^\circ$ of monovalent anions are at least 3 times lower than multivalent anions. The lower $\Delta_{\text{hyd}}G^\circ$ means the water molecules are loosely bonded with

the anions to form an unstable hydration structure, making these anions in bare rather than hydrated forms when they interact with the membrane. These exposed charges form a stronger repulsion force with the negatively charged surface of the ZC membrane, resulting in higher Na⁺/anion selectivity. Comparing monovalent anions among each other, they only have slightly different hydration energies, and the power density seems to follow the combined effects of the diffusion coefficient and hydration energy. We know that lower values of both diffusion coefficients and hydration energies of anions will result in higher Na⁺/anion selectivity. The diffusion coefficients follow the trend of OH⁻ > Br⁻ > I⁻ > Cl⁻ > NO₃⁻ > F⁻ (Supplementary Table 2), while the hydration energy represents a decreasing order of F⁻ > OH⁻ > Cl⁻ > Br⁻ > NO₃⁻ > I⁻ (Supplementary Table 3). Combining the effects of these two factors, the osmotic power densities have a ranking of F⁻ > I⁻ > Br⁻ > NO₃⁻ > OH⁻ > Cl⁻ (Supplementary Fig. 21), with a power density of -41.2 W m⁻² in NaF. However, for multivalent anions, the power density ranking (S²⁻ > PO₄³⁻ > SO₄²⁻ > CO₃²⁻) correlates with neither diffusion coefficient nor hydration energy. A careful literature study found it follows the reverse order of the Hofmeister series (CO₃²⁻ > SO₄²⁻ > PO₄³⁻ > S²⁻)⁴⁶, which ranks the ability of anions to salt out proteins. Though the exact mechanism of the Hofmeister series was not entirely clear thus far, it seems to relate to the Coulombic interactions between the hydrated anions and water⁴⁷. For example, CO₃²⁻ could polarize water molecules and form a stable water-anion structure in aqueous solution. As a result, the negative charges of CO₃²⁻ are well-shielded by the surrounding waters and cannot screen the repulsion forces between the heads of protein, leading to protein aggregation and precipitation (salting-out effects)⁴⁶. Such effects could also explain the interaction of anions with the negatively charged surface of the ZC membrane. The

highly shield CO_3^{2-} are unable to be repelled by the charged surface, making them easily to enter and diffuse through the sub-nanofluidic channels together with Na^+ . This leads to a poorer Na^+ /anion selectivity and lower osmotic power density (Na_2CO_3 , 1.0 W m^{-2}). Such low osmotic power density of CO_3^{2-} (high diffusion rate) indicates the ZC membrane can separate CO_3^{2-} from anions that generate higher osmotic power density (lower diffusion rate), resulting in a selectivity of 25.3, 19.6, 13.38 for $\text{CO}_3^{2-}/\text{OH}^-$, $\text{CO}_3^{2-}/\text{Cl}^-$, and $\text{CO}_3^{2-}/\text{PO}_4^{3-}$ respectively (Fig. 5b).

Osmotic power generation in practical conditions

Besides the types of anions and cations discussed above, pH is also an important factor that can affect osmotic power generation in the ZC membrane. It is clear that the power density increased as the pH of the NaCl electrolyte increased from 4.17 to 12.08 (Fig. 5c, Supplementary Fig. 23). This is within expectation and has been seen in other reported cation-selective membranes^{2,37}. The surface charge density $\sigma_{D,zp}$ increased with increased pH on the ZC membrane (Supplementary Fig. 22), leading to both stronger attraction towards Na^+ and repulsion towards Cl^- . Such intensified electrical force results in higher cation/anion selectivity, hence greater power density. In particular, the ZC membrane also exhibited an excellent power density (26.3 W m^{-2}) in pure NaOH electrolyte (0.5 M:0.01 M). The impressive performance in such a concentrated alkaline solution and the ability to separate CO_3^{2-} from other types of anions, to our best knowledge, has never been reported so far. These properties demonstrate the ZC membrane can be used in highly alkaline conditions. In the real world, besides alkalinity, water always has various salt concentrations depending on the source origins. Taking this into consideration, we tested the membrane's performance in various concentration gradients of NaCl electrolytes (Supplementary Figs. 24 and 25). The osmotic power increased as the concentration gradient increased from 50 to 500 and achieved -121 W m^{-2} at 500-fold. We further evaluate the membrane's performance in practical conditions (Fig. 5d, Supplementary Fig. 26, and Supplementary Table 6), and it achieved a power density of 29.1 W m^{-2} , 81.0 W m^{-2} , and 380.1 W m^{-2} in waters of the Red Sea/River, Dead Sea/River, and Qinghai Brine/River, respectively. Such impressive performance demonstrates the ZC membrane's high potential in blue energy conversion under real-world conditions. The membrane also had good stability and could sustain the performance with slight deterioration in seven days of testing under artificial seawater/river water conditions (50-fold) under both static (Fig. 5e) and (Supplementary Fig. 27) continuous testing conditions. We also studied the effects of membrane area on the performance. The power density decreased as the area increased (Supplementary Fig. 28). This is a common observation by many publications, as can be seen in the graph summarizing the reported power density versus the tested area (Supplementary Fig. 29). This phenomenon can be attributed to multiple factors including the increased entry resistance, lower counter-ion diffusion, and stochastic defects⁴. Finally, we compared the power density of the ZC membrane with the reported state-of-art membranes tested in the same area and conditions. Our results sit at the upper right. It highlights the unprecedented performance of the ZC membrane in blue energy conversion. In addition, our membrane can be easily fabricated into large areas (Supplementary Fig. 30) with impressive mechanical strength under flexible bending, making it attractive for industrial scale-up.

Summary

In summary, this report has convincingly demonstrated that NaX zeolite can serve as a high-performing membrane for blue energy generation, with a remarkable power density of 21.27 W m^{-2} achieved under a 50-fold NaCl concentration gradient. The testing was conducted in various practical scenarios, including the Red Sea/River, Dead Sea/River, and Qinghai Brine/River, further showcasing its

exceptional performance, yielding power densities of 29.1 W m^{-2} , 81.0 W m^{-2} , and 380.1 W m^{-2} , respectively. The adaptability of this zeolite membrane to high alkaline conditions (-0.5 M NaOH) and its ability to separate CO_3^{2-} from OH^- ions with a selectivity of 25 underscore its potential in blue energy conversion under harsh conditions. In addition, the membrane can be easily fabricated in large areas and exhibited impressive mechanical stability under flexible bending, highlighting its vast potential for real-industrial scale-up. These results underscore the significant promise of zeolite membranes in revolutionizing blue energy generation, paving the way for broader and more impactful applications of zeolite in this innovative field.

Methods

Zeolite membrane synthesis

The synthesis precursor was made based on a previous report⁴⁸ with some modifications. To prepare the synthesis precursor, aluminate solution and silica solution were made separately before mixing. The aluminate solution was prepared by dissolving 3 g of aluminum foil and 311.2 g of sodium hydroxide in 1000 g of water, then stirring at room temperature until a clear solution formed. The silica solution was prepared by mixing 166.8 g of LUDOX AS-40 colloidal silica with 889 g of water, then sonicating at room temperature until a homogeneous solution formed. Then the silica solution was poured into the aluminate solution and stirred at room temperature overnight until a clear solution was formed. The clear solution, with a molar composition of $70\text{Na}_2\text{O}:1\text{Al}_2\text{O}_3:20\text{SiO}_2:2000\text{H}_2\text{O}$, was used as the membrane synthesis precursor. Based on this molar composition, the concentration of each reactant can be obtained. We prepare 2 L of this precursor and get $\sim 50 \text{ mL}$ for one membrane synthesis. To fabricate a membrane, the prepared CNT-supported substrate was placed horizontally (CNT side facing downward) in a Teflon-lined stainless-steel autoclave filled with the synthesis precursor. Then, the autoclave was heated at 75°C for 14 h. After hydrothermal growth, the formed ZC membrane was taken out and thoroughly washed with deionized water to remove reactants and dried at room temperature.

Membrane characterizations

XRD patterns were taken using a Bruker D8 ADVANCE Twin diffractometer (40 kV, 40 mA, Cu K α radiation, 0.01° 2θ step size). The instrument was calibrated using a standard $\alpha\text{-Al}_2\text{O}_3$ specimen, with a reference peak at $2\theta = 35.15 \pm 0.01^\circ$. XPS testing was performed on a Kratos AXIS Ultra DLD system equipped with a monochromatic X-ray source and a dual Al-Mg anode. Peak energies were calibrated using the adventitious carbon C1s peak, which is centered at 284.8 eV. FTIR spectroscopy was carried out on a Thermo Scientific Nicolet iS10 machine using the attenuated total reflection mode. Background correction was performed every 30 min by acquiring a reference spectrum without a sample, to compensate for environmental interferences such as water vapor and carbon dioxide. Raman spectra were recorded on a Witec alpha300 Apyron confocal microscope with a 532-nm source (coherent compass sapphire laser) at 5–30 mW power. System calibration was verified by confirming the peak of a single-crystalline silicon sample at 521 cm^{-1} . Solid-state nuclear magnetic resonance (ssNMR) spectroscopy was conducted using a Bruker 600 M WB Solid NMR spectrometer system. SEM images were captured using a Zeiss Merlin SEM machine operated at 5 kV and 70 pA. Low-dose HRTEM was performed on a Cs-corrected FEI cubed G2 Titan 60–300 electron microscope at 300 kV, using a Gatan K2 direct-detection camera in electron counting mode. AFM images were obtained from a Bruker Dimension Icon AFM instrument. N_2 adsorption/desorption isotherms at 77 K were obtained using a Micromeritics ASAP 2020 analyzer. Prior to measurement, the samples were degassed under vacuum at 200°C for 12 h. The pore size distribution of the samples was calculated using the non-local density functional theory (NLDFT) carbon slit model based on the N_2 isotherms.

Surface charge calculation

The apparent surface charge density is estimated from zeta potential with Eq. (1) below.

$$\sigma_{D,zp} = \frac{\varepsilon\varepsilon_0\xi}{\lambda_D} \quad (1)$$

$\sigma_{D,zp}$: Surface charge density of particles, ε : Static dielectric constant of pure water, ε_0 : Permittivity of free space, ξ : Zeta potential, λ_D : Debye length of the electrolyte. The Debye length of the electrolyte is obtained by Eq. (2).

$$\lambda_D = \sqrt{\frac{\varepsilon\varepsilon_0RT}{2nF^2C_0}} \quad (2)$$

λ_D : Debye length, ε : Static dielectric constant of pure water, ε_0 : Permittivity of free space, R: Gas constant, T: Absolute temperature: Valent number, F: Faraday constant, C_0 : Electrolyte concentration.

Since the measurement conducted in this study was carried out at room temperature and the electrolyte used was monovalent, Eq. (2) can be simplified into Eq. (3).

$$\lambda_D = \frac{0.304}{\sqrt{C_0}} \quad (3)$$

C_0 : Electrolyte concentration (M or mol L⁻¹)

Combining Eqs. (1) and (3), the surface charge density can be obtained by Eq. (4).

$$\sigma_{D,zp} = \frac{\varepsilon\varepsilon_0\xi\sqrt{C_0}}{0.304} \times 10^9 \quad (4)$$

$\sigma_{D,zp}$: Surface charge density of particles at 293 K (mC m⁻²), ε : Static dielectric constant of pure water at 293 K, ε_0 : Permittivity of free space, ξ : Zeta potential (in mV), C_0 : Electrolyte concentration (in M or mol L⁻¹).

Ion transport measurement

The ZC membrane was mounted in a homemade electrochemical cell, and sealed using a water-resistant epoxy glue to make the effective membrane area to be ~0.03 mm². The accurate area was measured by a Keyence VH-Z100R Camera. Before measurement, the membrane was wetted by the electrolyte filled in the two chambers for 30 s twice. The electrolyte was replenished between each wetting process. A pair of Ag/AgCl electrodes (diameter: ~0.5 mm) with salt bridges (saturated KCl solution) were immersed into the electrolyte solution of the two chambers and connected to an electrochemical station (CHI 660E). A voltage bias from -0.5 V to 0.5 V was applied to measure the current generated across the membrane. For conductance measurement, the two chambers were filled with electrolytes (KCl or NaCl) of the same concentration. The concentration varied from 10⁻⁶ M to 1 M. The conductance was calculated by fitting the measured I-V curve. For osmotic bias measurement, two chambers were charged with electrolytes with a concentration gradient. Similar to conductance measurement, a voltage bias between -0.5 V and 0.5 V was applied to collect the I-V data. The osmotic current (I_{os}) and voltage (V_{os}) were obtained from reading the I-V curve interception with the zero point on the axis. Using the obtained V_{os} , the transference number t^+ can be calculated based on Eq. (5) below.

$$2t^+ = \frac{V_{os}}{\left(\frac{RT}{F}\right)\ln\left(\frac{\gamma_h C_h}{\gamma_l C_l}\right)} + 1 \quad (5)$$

t^+ : Transference number of cations, V_{os} : Osmotic potential, R: Gas constant, T: Absolute temperature, F: Faraday constant, γ_h : Activity coefficient of electrolyte with high concentration, γ_l : Activity

coefficient of electrolyte with low concentration, C_h : Electrolyte concentration (high concentration side), C_l : Electrolyte concentration (low concentration side).

Here, the activity coefficient γ of electrolyte in both high and low concentration sides was assumed to be one. Thus, Eq. (5) can be simplified into Eq. (6).

$$2t^+ = \frac{V_{os}}{\left(\frac{RT}{F}\right)\ln\left(\frac{C_h}{C_l}\right)} + 1 \quad (6)$$

Since the sum of the transference number of cations (t^+) and anions (t^-) is equal to one, t^- can be obtained by subtracting one by t^+ . Then, the cation/anion selectivity can be calculated based on Eq. (7).

$$\text{Cation/Anion, Selectivity} = \frac{t^+}{t^-} \quad (7)$$

Based on the calculated cation transference number t^+ , the energy conversion efficiency η can be obtained from Eq. (8).

$$\eta = \frac{(2t^+ - 1)^2}{2} \times 100\% \quad (8)$$

Osmotic power generation

The setup for osmotic power measurement is the same as the ion transport measurement except that the homemade electrochemical cell was connected to an external load resistor (MC-21-B, Mingcheng, Shenzhen, China). The current was measured by a source meter (KEITHLEY, 2450 SourceMeter®). For each measurement at a given resistance, the current was recorded until it stabilized. The power density P was calculated by Eq. (9).

$$P = I^2 R / A \quad (9)$$

P: Osmotic power density, I: Current, R: Resistance, A: Membrane area.

Data availability

The authors declare that the data supporting the findings of the study are included in the main text and supplementary information files. Raw data can be obtained from the corresponding author upon request.

References

- Xu, Y., Song, Y. & Xu, F. TEMPO oxidized cellulose nanofibers-based heterogeneous membrane employed for concentration-gradient-driven energy harvesting. *Nano Energy* **79**, 105468 (2021).
- Xin, W. et al. High-performance silk-based hybrid membranes employed for osmotic energy conversion. *Nat. Commun.* **10**, 3876 (2019).
- Zhou, S. et al. Interfacial super-assembly of ordered mesoporous carbon-silica/AAO hybrid membrane with enhanced permselectivity for temperature- and pH-sensitive smart ion transport. *Angew. Chem.* **133**, 26371–26380 (2021).
- Zhang, Z. et al. Improved osmotic energy conversion in heterogeneous membrane boosted by three-dimensional hydrogel interface. *Nat. Commun.* **11**, 875 (2020).
- Cao, L. et al. Giant osmotic energy conversion through vertical-aligned ion-permeable nanochannels in covalent organic framework membranes. *J. Am. Chem. Soc.* **144**, 12400–12409 (2022).
- Cao, L. et al. An Ionic Diode Covalent Organic Framework Membrane for Efficient Osmotic Energy Conversion. *ACS nano* **16**, 18910–18920 (2022).
- Zhang, Z. et al. Mechanically strong MXene/Kevlar nanofiber composite membranes as high-performance nanofluidic osmotic power generators. *Nat. Commun.* **10**, 2920 (2019).

8. Fu, Y., Guo, X., Wang, Y., Wang, X. & Xue, J. An atomically-thin graphene reverse electro dialysis system for efficient energy harvesting from salinity gradient. *Nano Energy* **57**, 783–790 (2019).
9. Morth, J. P. et al. Crystal structure of the sodium–potassium pump. *Nature* **450**, 1043–1049 (2007).
10. Xu, J. & Lavan, D. A. Designing artificial cells to harness the biological ion concentration gradient. *Nat. Nanotechnol.* **3**, 666–670 (2008).
11. Jian, M. et al. Ultrathin water-stable metal-organic framework membranes for ion separation. *Sci. Adv.* **6**, eaay3998 (2020).
12. Li, R., Jiang, J., Liu, Q., Xie, Z. & Zhai, J. Hybrid nanochannel membrane based on polymer/MOF for high-performance salinity gradient power generation. *Nano Energy* **53**, 643–649 (2018).
13. Wang, C. et al. Fabrication of Bio-Inspired 2D MOFs/PAA Hybrid Membrane for Asymmetric Ion Transport. *Adv. Funct. Mater.* **30**, 1908804 (2020).
14. Liu, Y.-C., Yeh, L.-H., Zheng, M.-J. & Wu, K. C.-W. Highly selective and high-performance osmotic power generators in sub-nanochannel membranes enabled by metal-organic frameworks. *Sci. Adv.* **7**, eabe9924 (2021).
15. Davis, M. E. Ordered porous materials for emerging applications. *Nature* **417**, 813–821 (2002).
16. Li, X. et al. Machine learning-assisted crystal engineering of a zeolite. *Nat. Commun.* **14**, 3152 (2023).
17. Kumar, P. et al. One-dimensional intergrowths in two-dimensional zeolite nanosheets and their effect on ultra-selective transport. *Nat. Mater.* **19**, 443–449 (2020).
18. Urtiaga, A., Gorri, E., Casado, C. & Ortiz, I. Pervaporative dehydration of industrial solvents using a zeolite NaA commercial membrane. *Sep. Purif. Technol.* **32**, 207–213 (2003).
19. Rangnekar, N., Mittal, N., Elyassi, B., Caro, J. & Tsapatsis, M. Zeolite membranes—a review and comparison with MOFs. *Chem. Soc. Rev.* **44**, 7128–7154 (2015).
20. Chi, X. et al. A highly stable and flexible zeolite electrolyte solid-state Li–air battery. *Nature* **592**, 551–557 (2021).
21. Breck, D. W. Zeolite molecular sieves: structure, chemistry, and use (John Wiley, New York, 1974).
22. Ezzeddine, Z., Batonneau-Gener, I. & Pouilloux, Y. Cation exchange mechanism of divalent metals ions in synthetic NaX and LTA zeolites: efficiency and selectivity. *Eur. Chem. Bull.* **7**, 93–98 (2018).
23. Panek, R. et al. Simultaneous removal of Pb²⁺ and Zn²⁺ heavy metals using fly ash Na-X zeolite and its carbon Na-X (C) composite. *Materials* **14**, 2832 (2021).
24. Awala, H. et al. Template-free nanosized faujasite-type zeolites. *Nat. Mater.* **14**, 447–451 (2015).
25. Zhou, Z. et al. Electropolymerization of robust conjugated microporous polymer membranes for rapid solvent transport and narrow molecular sieving. *Nat. Commun.* **11**, 5323 (2020).
26. Wei, R. et al. Carbon nanotube supported oriented metal organic framework membrane for effective ethylene/ethane separation. *Sci. Adv.* **8**, eabm6741 (2022).
27. Zhan, G.-D., Kuntz, J. D., Wan, J. & Mukherjee, A. K. Single-wall carbon nanotubes as attractive toughening agents in alumina-based nanocomposites. *Nat. Mater.* **2**, 38–42 (2003).
28. Ning, J., Zhang, J., Pan, Y. & Guo, J. Fabrication and mechanical properties of SiO₂ matrix composites reinforced by carbon nanotube. *Mater. Sci. Eng. A* **357**, 392–396 (2003).
29. Huang, M., Adnot, A. & Kaliaguine, S. Cation-framework interaction in alkali-cation-exchanged zeolites: an XPS study. *J. Am. Chem. Soc.* **114**, 10005–10010 (1992).
30. Xiong, G. et al. UV Raman spectroscopic study on the synthesis mechanism of zeolite X. *Microporous Mesoporous Mater.* **42**, 317–323 (2001).
31. Coudurier, G., Naccache, C. & Vedrine, J. C. Uses of IR spectroscopy in identifying ZSM zeolite structure. *J. Chem. Soc. Chem. Commun.* <https://doi.org/10.1039/C39820001413>, 1413–1415 (1982).
32. Barr, T. L. The nature of the relative bonding chemistry in zeolites: an XPS study. *Zeolites* **10**, 760–765 (1990).
33. Flanigen E. M., Khatami H., Szymanski HA. Infrared structural studies of zeolite frameworks.) ACS Publications (1971).
34. Beyer, H. K. et al. Preparation of high-silica faujasites by treatment with silicon tetrachloride. *J. Chem. Soc. Faraday Trans. 1 Phys. Chem. Condens. Phases* **81**, 2889–2901 (1985).
35. Kubelková, L., Seidl, V., Borbély, G. & Beyer, H. K. Correlations between wavenumbers of skeletal vibrations, unit-cell size and molar fraction of aluminium of Y zeolites. Removal of non-skeletal al species with H₂Na₂EDTA. *J. Chem. Soc. Faraday Trans. 1 Phys. Chem. Condens. Phases* **84**, 1447–1454 (1988).
36. Karge, H. G., Hunger, M. & Beyer, H. K. Characterization of zeolites—Infrared and nuclear magnetic resonance spectroscopy and X-ray diffraction. In: *Catalysis and zeolites: Fundamentals and applications* (Springer, 1999).
37. Zhang, Z. et al. Cation-selective two-dimensional polyimine membranes for high-performance osmotic energy conversion. *Nat. Commun.* **13**, 3935 (2022).
38. Zhang, Z. et al. Oxidation promoted osmotic energy conversion in black phosphorus membranes. *Proc. Natl Acad. Sci.* **117**, 13959–13966 (2020).
39. Janusz, W. Electrical double layer at the metal oxide-electrolyte interface. *Surfactant Sci. Ser.* **85**, 135–206 (1999).
40. Rahman, M. M. Membranes for Osmotic Power Generation by Reverse Electrodialysis. *Membranes* **13**, 164 (2023).
41. Gao, J. et al. High-performance ionic diode membrane for salinity gradient power generation. *J. Am. Chem. Soc.* **136**, 12265–12272 (2014).
42. Zhang, Z. et al. Ultrathin and ion-selective Janus membranes for high-performance osmotic energy conversion. *J. Am. Chem. Soc.* **139**, 8905–8914 (2017).
43. Lin, C.-Y. et al. Modulation of charge density and charge polarity of nanopore wall by salt gradient and voltage. *ACS Nano* **13**, 9868–9879 (2019).
44. Fu, L., Wang, Y., Jiang, J., Lu, B. & Zhai, J. Sandwich “Ion Pool”-Structured Power Gating for Salinity Gradient Generation Devices. *ACS Appl. Mater. Interfaces* **13**, 35197–35206 (2021).
45. Esfandiari, A. et al. Size effect in ion transport through angstrom-scale slits. *Science* **358**, 511–513 (2017).
46. Gregory, K. P. et al. Understanding specific ion effects and the Hofmeister series. *Phys. Chem. Chem. Phys.* **24**, 12682–12718 (2022).
47. Gregory, K. P., Wanless, E. J., Webber, G. B., Craig, V. S. & Page, A. J. The electrostatic origins of specific ion effects: quantifying the Hofmeister series for anions. *Chem. Sci.* **12**, 15007–15015 (2021).
48. Zhu, G., Li, Y., Zhou, H., Liu, J. & Yang, W. FAU-type zeolite membranes synthesized by microwave assisted in situ crystallization. *Mater. Lett.* **62**, 4357–4359 (2008).
49. Frising, T. & Leflaive, P. Extraframework cation distributions in X and Y faujasite zeolites: A review. *Microporous Mesoporous Mater.* **114**, 27–63 (2008).

Acknowledgements

We acknowledge financial support by King Abdullah University of Science and Technology BAS/1/1375-01-01.

Author contributions

R.W., X.L., and Z.L. conceived the research concept, formulated experimental designs, and wrote the manuscript. Experimental work and data analysis were conducted by R.W., X.L., and L.C., with collaborative support from C.C., I.C., Z.L., and J.M. All authors actively participated in data discussions and provided feedback on the manuscript.

Competing interests

The authors declare no competing interests.

Additional information

Supplementary information The online version contains supplementary material available at <https://doi.org/10.1038/s41467-024-54755-4>.

Correspondence and requests for materials should be addressed to Zhiping Lai.

Peer review information *Nature Communications* thanks Mohsen Asadnia, Kalyan Raidongia and the other, anonymous, reviewer for their contribution to the peer review of this work. A peer review file is available.

Reprints and permissions information is available at <http://www.nature.com/reprints>

Publisher's note Springer Nature remains neutral with regard to jurisdictional claims in published maps and institutional affiliations.

Open Access This article is licensed under a Creative Commons Attribution-NonCommercial-NoDerivatives 4.0 International License, which permits any non-commercial use, sharing, distribution and reproduction in any medium or format, as long as you give appropriate credit to the original author(s) and the source, provide a link to the Creative Commons licence, and indicate if you modified the licensed material. You do not have permission under this licence to share adapted material derived from this article or parts of it. The images or other third party material in this article are included in the article's Creative Commons licence, unless indicated otherwise in a credit line to the material. If material is not included in the article's Creative Commons licence and your intended use is not permitted by statutory regulation or exceeds the permitted use, you will need to obtain permission directly from the copyright holder. To view a copy of this licence, visit <http://creativecommons.org/licenses/by-nc-nd/4.0/>.

© The Author(s) 2024